Inorganic Chemistry

pubs.acs.org/IC

Article

$Fe_{0.6}Pd_{0.4}Te_2$: A New Polymorph of $FeTe_2$ and $PdTe_2$ Stable at Ambient Pressure

Wanping Wang, Jianjun Tian,* Xiao Tong,* Michael O. Ogunbunmi, Yang Fu, Zhixiang Hu, Svilen Bobev, Zeljko Sljivancanin, Hechang Lei, Weifeng Zhang, and Cedomir Petrovic*

Cite This: *Inorg. Chem.* 2025, 64, 23825−23833

Read Online

ACCESS | Metrics & More | Article Recommendations

ABSTRACT: Although the pyrite space group is a high-pressure polymorph of $FeTe_2$, here we report $Fe_{0.6}Pd_{0.4}Te_2$ with the pyrite space group Pa-3 prepared using Pd substitution on the Fe atomic site with ambient pressure crystal growth methods. $Fe_{0.6(1)}Pd_{0.4(1)}Te_2$ single crystals show metal behavior above 15 K abided by the Bloch−Grüneisen relation and display resistivity upturn below 15 K due to disorder-related scattering of correlated electronic states.

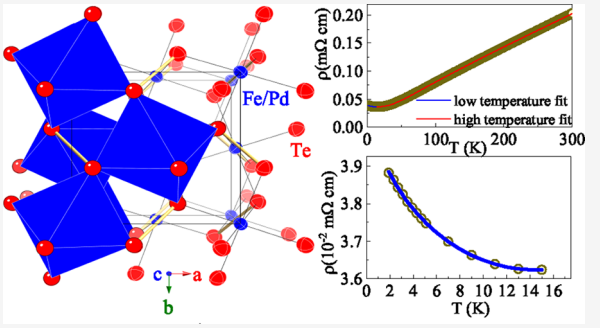

INTRODUCTION

Transition-metal dichalcogenides (TMDCs) display a great variety of physical properties, including superconductivity,[1−4] Mott-insulator to metal transition,[5] charge-density wave,[6] and spin glass behavior.[7] $FeTe_2$ and $PdTe_2$ crystallize in marcasite *Pnnm* (space group No. 58) and CdI_2-type space group $P\bar{3}m1$ (No. 164), respectively.[8,9] They are synthesized by heating at 1073 K for several days ($FeTe_2$) or by adding Te to PdTe and annealing at 573 K in an evacuated quartz tube for 30 days ($PdTe_2$), whereas pyrite-type $FeTe_2$ is synthesized only at high pressure by heating to 1100 K, cooling to 400 K, and then quenching to room temperature.[8−10] $PdTe_2$ not only features an *s*-wave superconducting ground state below 1.69 K but also hosts pressure-tunable type-II Dirac Fermions and exhibits superior chemical and thermal stability of interest for optoelectronic devices and detection in infrared and terahertz ranges.[11−22] $PdTe_2$ nanosheets exhibit 5-fold activity when compared to that of commercial Pd, making it a rather promising electrocatalyst material for high-performance energy conversion.[23] Enhanced catalytic activity is also obtained in defect-engineered $PdTe_2$ crystals.[24] Marcasite $FeTe_2$ with vacancy defects on Fe atomic sites is a paramagnetic metal with low thermal conductivity, whereas for full occupancy of Fe, it shows antiferromagnetic transition at 79 K and ferromagnetic below 35 K.[25,26] $FeTe_2$ is of interest as cathode materials in nanocomposites for aluminum-ion batteries due to extremely long-time cycle performance.[27] Pyrite $FeTe_2$ is a semimetal with a small effective moment.[10] Given the recently recognized importance of pyrite-type materials in energy applications, it is of interest to explore new pyrite structures.[28−30]

Pyrite-type crystal structures are characterized by the face-centered cubic (fcc) AB_2 lattice where frustration of magnetic interactions generated by moments arising from localized electronic states/orbitals of rock-salt-arranged A atoms is well-known, particularly when the next-nearest-neighbor interaction is important.[31−34] Interestingly, chemical alloying may induce a significant change in bond energies and enthalpies of formation so that the high-pressure polymorph is stabilized even at ambient pressure, resulting in new functionalities. For example, $Fe_{0.33}Pd_{0.67}Se_2$ in pyrite structure type displays metal-like and magnetic spin-glass behaviors below 18 K and is stable at ambient pressure, even though the pyrite structure is a high-pressure polymorph for both $FeSe_2$ and $PdSe_2$.[35] These studies indicate possible crystal structure changes and property tuning of $PdTe_2$ by cationic substitutions.

Here, we report the synthesis and characterization of $Fe_{0.6(1)}Pd_{0.4(1)}Te_2$ single crystals with the pyrite space group $Pa\bar{3}$. To the best of our knowledge, the pyrite-type polymorph of $FeTe_2$ is synthesized for the first time under ambient conditions; the polymorphic phase is induced by Pd substitution. Our studies indicate a paramagnetic metal state

Received: June 17, 2025
Revised: October 25, 2025
Accepted: October 28, 2025
Published: December 1, 2025

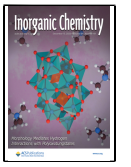

with an interplay of disorder and enhanced electronic correlations at low temperatures.

EXPERIMENTAL SECTION

Synthesis. Single crystals of $Fe_{0.6(1)}Pd_{0.4(1)}Te_2$ were grown from Te-rich melt with Fe:Pd:Te with a 1:x:10 mol ratio, with the pyrite-type structure forming only when x = (1−2). The source elements were put into an alumina crucible and then sealed in a quartz tube with a partial pressure of argon gas. The heating temperature for the tube was ramped slowly to 900 °C. After brief 3 h soaking, the quartz tube was cooled to 500 °C over 150 h, at which point crystals were decanted from the liquid in a centrifuge. Excess Te was filtered out by decanting through quartz wool.[36−39] Shiny single crystals of up to 1.6 × 1.5 × 1.4 mm^3 can be grown.

Composition and Structural Analysis. Chemical compositions were investigated by energy-dispersive X-ray spectroscopy (EDX) in a JEOL LSM-7900F scanning electron microscope. To confirm phase purity, powder X-ray diffraction data of the sample were collected by a Rigaku Miniflex X-ray diffractometer with Cu K_α radiation (λ = 1.55406 Å). The unit cell was refined using RIETICA software.[40] For single-crystal X-ray diffraction, crystals were selected under a microscope and cut to dimensions of 0.10 × 0.10 × 0.089 mm^3. They were mounted on low-background plastic holders using Paratone N oil, transferred to a goniometer, and placed under a cold stream of nitrogen gas (ca. 200 K). Data acquisitions took place on a Bruker APEX II CCD diffractometer using graphite-monochromatized Mo K_α radiation (λ = 0.71073 Å). A total of 971 reflections were collected ($2\theta_{max} \sim 60°$), 138 of which were unique (T_{min}/T_{max} = 0.173/0.195, R_{int} = 0.034). The data collection, data reduction and integration, and refinement of the cell parameters were carried out using the Bruker-provided programs (SAINT; Bruker AXS Inc., Madison, Wisconsin, USA, 2014). Semiempirical absorption correction was applied with the aid of the SADABS software package (SADABS; Bruker AXS Inc., Madison, Wisconsin, USA, 2014). The structure was subsequently solved by direct methods and refined on F^2 (8 parameters) with the aid of the SHELXL package.[41] All atoms were refined with anisotropic displacement parameters with scattering factors (neutral atoms) and absorption coefficients.[42]

Electrical, Magnetic, and Thermodynamic Measurements. Electrical transport and magnetization measurements were carried out in Quantum Design (QD) PPMS-9 and MPMS-XL instruments. For resistivity measurement, crystals were polished into a rectangular shape. Silver paint and thin Pt wires were used to create contacts with about 10−20 Ohm contact resistance. Resistivity was measured using an LR 700 resistance bridge with a 16 Hz excitation frequency. Magnetic measurements were conducted using QD-provided straw sample holders. Heat capacity was measured in QD PPMS-9 using a standard QD relaxation method.

X-ray and Ultraviolet Photoelectron Spectroscopy. Our X-ray photoelectron spectroscopy (XPS) and ultraviolet photoelectron spectroscopy (UPS) experiments were carried out in an ultrahigh vacuum (UHV) system with base pressures less than 2 × 10^{-9} Torr, equipped with a hemispherical electron energy analyzer (SPECS, PHOIBOS 100) and twin anode X-ray source (SPECS, XR50) with Al K_a (1486.7 eV) radiation at 10 kV and 30 mA, as well as an ultraviolet source (SPECS, 10/35) He(I) at 21.2 eV radiation. The angle between the analyzer and X-ray source (and UV source) was 45°. XPS/UPS data were collected along the sample surface normal before and after Ar^+ sputtering. Samples were sputtered under an Ar gas pressure of 2 × 10^{-5} Torr with 2 keV kinetic energy of Ar^+ ions for 40 min. The data were analyzed using Casa XPS. The XPS peak positions were calibrated using adventitious carbon C 1s at 248.5 eV. The UPS spectra were calibrated vs the Fermi edge of the Au(111) crystal. To obtain a clear and accurate secondary electron emission cutoff for work function measurement, the sample was electrically biased by −10 V relative to the photoelectron energy analyzer.

Electronic Structure Calculations. To get insight into the effect of Pd doping on the electronic properties and charge distribution in $Fe_{0.6}Pd_{0.4}Te_2$, we performed density functional theory (DFT) calculations, using the GPAW code.[43] Starting from the conventional cubic unit cell (space group $Pa\bar{3}$), we constructed a 2 × 2 × 2 supercell containing 32 Fe and 64 Te atoms, which provides sufficient size to model the disordered Pd/Fe distribution. To match the experimental stoichiometry, 12 randomly selected Fe sites were substituted with Pd, yielding the composition $Fe_{0.625}Pd_{0.375}Te_2$. We generated five distinct atomic configurations with the same Pd:Fe ratio but different Pd arrangements in order to verify that our conclusions are robust against variations in the dopant distribution. All calculations employed the experimental lattice constant of 6.442 Å, with atomic positions fully relaxed using the BFGS algorithm.[44] The valence electrons of Fe, Pd, and Te were described using the projector augmented-wave (PAW) method[45,46] and a plane-wave basis set with an energy cutoff of 600 eV. Exchange-correlation effects were treated within the PBE-GGA approximation,[47] and Brillouin zone sampling was performed using a 3 × 3 × 3 Monkhorst−Pack k-point grid.[48] Atomic charges were evaluated via Bader charge analysis.[49]

RESULTS AND DISCUSSION

Crystal Structure and Stoichiometry. Powder XRD data at room temperature are shown in Figure 1a. The data were taken on pulverized single crystals (Figure 1a inset). The unit cell (Figure 1b) is refined in the pyrite structure with space group $Pa\bar{3}$, and lattice constant a = 6.4422(1) Å is larger than that of high-pressure pyrite $FeTe_2$ (a = 6.2937(1) Å), $Fe_{0.50}Ni_{0.50}Te_2$ (a = 6.3541(1) Å), or $Fe_{0.33}Pd_{0.67}Se_2$ (a = 6.0542(3) Å) synthesized using ambient pressure methods.[10,35,50] The average atom composition from the EDX spectrum confirms that the single crystal is homogeneous (Figure 1c). The measured Fe:Pd:Te atom ratio from multiple points on different crystals grown in multiple batches using the Fe:Pd:Te = 1:x:10 ratio was 0.53(5):0.49(4):2.00 for x = 1 and 0.50(7):0.50(7):2.00 when fixing the Te stoichiometry to be 2. We note that the ambient pressure synthesis of pyrite-type $Fe_{0.6(1)}Pd_{0.4(1)}Te_2$ is possible using a similar temperature profile to that of pyrite-type $Fe_{0.36(4)}Pd_{0.64(4)}Se_2$, albeit with higher maximal heating and decanting temperatures. On the other hand, the pyrite phase for Se-based materials forms with a wider range of Fe/Pd ratios in the starting element composition.[35] In contrast to binary $FeTe_2$ and $PdTe_2$ pyrite phases, pyrite-type $Fe_{0.6(1)}Pd_{0.4(1)}Te_2$ shows enhanced electrical conductivity and a similar absence of magnetic order.

In the single-crystal X-ray refinement, the occupancy of the Fe site when set free gave an unphysical deviation from unity of about 121(1)%. Therefore, in agreement with the EDX data, Pd was introduced and refined together with Fe on the same site, showing a Fe:Pd random distribution with a ratio of Fe:Pd = 0.711(6):0.289. The discrepancy with EDX could reflect

https://doi.org/10.1021/acs.inorgchem.5c02764
Inorg. Chem. 2025, 64, 23825−23833

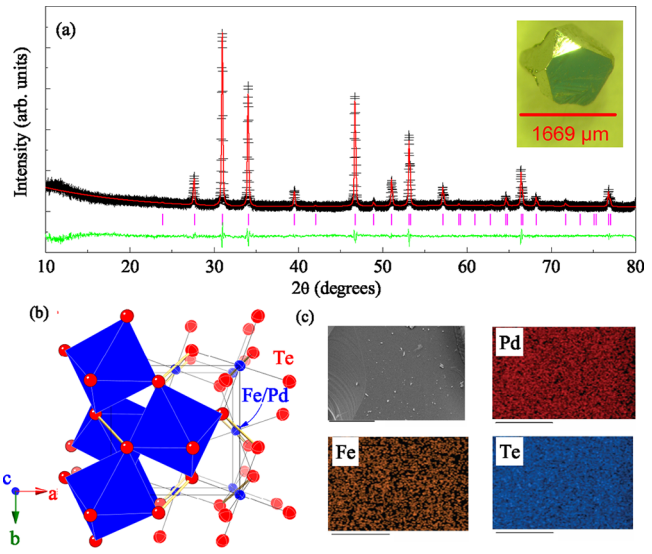

Figure 1. (a) Powder XRD patterns of $Fe_{0.6(1)}Pd_{0.4(1)}Te_2$ fit the $Pa\bar{3}$ model. Inset: typical single crystal. (b) Schematic view of the crystal structure projected down [001]. Displacement ellipsoids are drawn at the 95% probability level. The unit cell is outlined. The corner-shared octahedra of Te, centered by Fe or Pd atoms, are highlighted, together with the Te−Te dimers. In pyrite structures, each cation is coordinated by six anions in a slightly distorted octahedron, and the anion octahedra are connected by shared corners. Energy-dispersive spectroscopy (EDS) mapping (c) implies a homogeneous distribution of Fe, Pd, and Te. The black line below each subpanel is a 25 μm scale bar.

somewhat different Fe/Pd ratios among investigated crystals, i.e., $Fe_{0.6(1)}Pd_{0.4(1)}Te_2$ stoichiometry. The final Fourier map is featureless with the highest residual density of about 0.77e$^-$/Å^3, situated 1.1 Å away from Fe/Pd, and the deepest hole of about −0.70e$^-$/Å^3, situated 0.8 Å away from Fe/Pd. Further details of the data collection and structure refinements are given in Table 1, and the positional and equivalent isotropic displacement parameters are listed in Table 2. The final refined structure (pyrite type, Pearson index cP12) is shown in Figure 1b, with anisotropic displacement parameters drawn at the 99% probability level. Fe and Pd atoms share the same atomic site; each M atom (M = Fe/Pd) is coordinated by six Te atoms, forming a distorted MTe_6 octahedron due to the different radii between Fe and Pd atoms.

Table 1. Selected Single-Crystal Data Collection and Structure Refinement Parameters for $Fe_{0.72}Pd_{0.28}Te_2$ Measured at 200 K Using λ = 0.71073 Å[a]

refined composition	$Fe_{0.72(1)}Te_2$
formula mass (g/mol)	325.20
space group	$Pa\bar{3}$ (no. 205)
Z	4
a (Å)	6.4428(5)
V (Å^3)	267.44(4)
density (g cm^{-3})	8.08
$\mu_{MoK\alpha}$ (cm^{-1})	270.0
R_1 [$I > 2\sigma(I)$)][b]	0.017
wR_2 [$I > 2\sigma(I)$)][b]	0.035
$\Delta\rho_{max,min}$/e Å^{-3}	0.77, −0.70

[a]The corresponding crystallographic information file (CIF) has been deposited with the Cambridge Crystallographic Database Centre (CCDC), depository number 2473324. [b]$R_1 = \Sigma||F_o| - |F_c||/\Sigma|F_o|$, $wR_2 = [\Sigma[w(F_o^2 - F_c^2)^2]/\Sigma[w(F_o^2)^2]]^{1/2}$ where $w = 1/[\sigma^2F_o^2 + (0.0134 \times P)^2 + (0.0604 \times P)]$ and $P = (F_o^2 + 2F_c^2)/3$.

Table 2. Atomic Coordinates and Equivalent Displacement Parameters Å^2 of $Fe_{0.6(1)}Pd_{0.4(1)}Te_2$

atom	site	x	y	z	U_{eq}[a]
Fe/Pd[b]	4a	0	0	0	0.010(1)
Te	8c	0.37025(7)	x	x	0.014(1)

[a]U_{eq} is defined as one-third of the trace of the orthogonalized U_{ij} tensor. [b]Refined ratio Fe:Pd = 0.711(6):0.289.

Magnetic, Electrical, and Thermodynamic Properties. Magnetic properties of $Fe_{0.6}Pd_{0.4}Te_2$ are shown in Figure 2a,b.

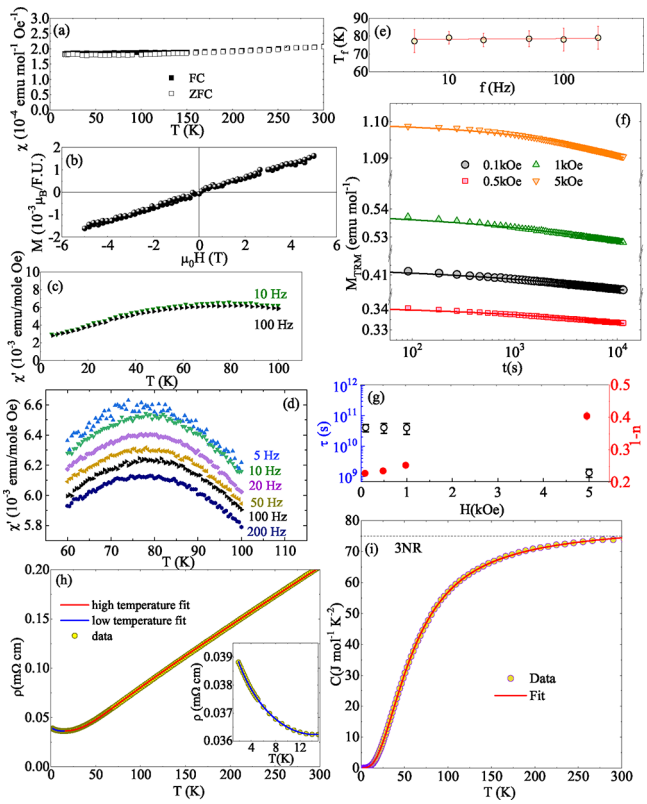

Figure 2. (a) Zero-field-cooled (ZFC) and field-cooled (FC) temperature-dependent magnetization measured in 1000 Oe parallel to the a axis. (b) Magnetic hysteresis curve at 5 K. Temperature dependence on ac susceptibility $\chi'(T)$ measured in the 5 Oe ac field (c,d). Frequency dependence of T_f (e). The solid line is the linear fit to the T_f data. (f) Time-dependent thermoremanent magnetization (TRM) at 10 K t_w = 100 s measured at the dc field with fittings using stretched exponential functions (solid lines, see the text). (g) Magnetic field dependences of $\tau(s)$ (full) and $1 - n$ (open symbols). (h) Temperature dependence of the resistivity ρ of single-crystal $Fe_{0.6(1)}Pd_{0.4(1)}Te_2$ from 1.8 to 300 K with Bloch−Grüneisen fit (solid line). The inset shows low-temperature regions with the corresponding fit (solid line, see the text). (i) Heat capacity fitted by the double-Debye model below room temperature.

We observe the absence of the long-range magnetic order, relatively large Pauli-like paramagnetic susceptibility, and a rather small magnetic hysteresis at 5 K. Very small hysteresis could arise due to impurities, defects, or intrinsic high-temperature magnetic order. Time-dependent ac magnetization is a good probe of magnetic spin glass systems since

https://doi.org/10.1021/acs.inorgchem.5c02764
Inorg. Chem. 2025, 64, 23825−23833

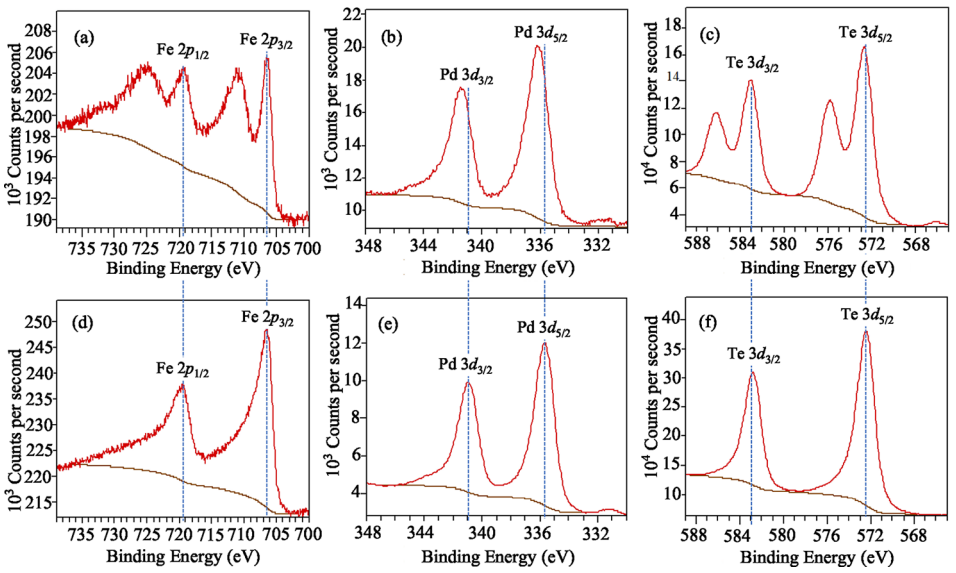

Figure 3. (a,d) Fe 2*p*, (b,e) Pd 3*d*, and (c,f) Te 3*d* XPS spectra obtained from $Fe_{0.6(1)}Pd_{0.4(1)}Te_2$ at room temperature before and after Ar ion sputtering.

spin interactions cause a highly irreversible metastable state. The real part of the ac susceptibility shows a weak frequency dependence (Figure 2c,d) in an applied ac magnetic field of 5 Oe, a relatively broad peak, and a decreasing magnitude of $\chi'(T)$, all consistent with magnetic spin glass behavior.[51] From the frequency dependence of the peak shift, we estimate $K = 0.0079(7)$ using $K = \Delta T_f/T_f \Delta \log f$ (Figure 3e), in agreement with the expected value range between 0.0045 and 0.08 of a spin glass system.[51] Another hallmark of spin glass, thermoremanent magnetization (M_{TRM}), is presented in Figure 2f. The sample was cooled from $T = 100$ K (above T_f) to 10 K (below T_f) in several different magnetic fields and then held for $t_w = 100$ s. The magnetization decay $M_{TRM}(t)$ was measured after the magnetic field was removed. We observe slow relaxation of $M_{TRM}(t)$ at 10 K, and nonzero values even after several hours (Figure 2f) also support the presence of spin glass interactions.[51] The decay is fitted with the formula $M_{TRM}(t) = M_0 \exp[-(t/\tau)^{1-n}]$, where M_0, τ, and $1 - n$ are the glassy component, the relaxation time, and the critical exponent, respectively. The τ decreases with the magnetic field increase up to 1 kOe, whereas the $1 - n$ value decreases with increasing H (Figure 3g). Obtained $1 - n$ is in line with the theoretical and experimental values found in other spin glass materials.[52]

Figure 2h shows the temperature dependence of the in-plane (ρ_{ab}) resistivity of $Fe_{0.6(1)}Pd_{0.4(1)}Te_2$ single crystals from 1.8 to 300 K. The sample exhibits metallic behavior on cooling at room temperature. Note that the resistivity linearly increases when T exceeds about 50 K and shows a resistance minimum at about 15 K. The generalized Bloch–Grüneisen model was used to express the contribution to the $\rho(T)$ of materials from the scattering of conduction electrons due to acoustic lattice vibrations:[53]

$$\rho(T) = \rho_0 + C\left(\frac{T}{\Theta_D}\right)^5 \int_0^{\Theta_D/T} \frac{x^5}{(e^x - 1)(1 - e^{-x})} dx \quad (1)$$

where ρ_0 is the residual resistivity from defects and impurities for $T \to 0$; C is a constant, reflecting the electron–phonon coupling strength; and Θ_D is the Debye temperature. The last term reflects the contributions from the electron–phonon interaction. Resistivity fit from 15 to 300 K (red line in Figure 2h) yields ρ_0, C, and Θ_D values of $3.6(6) \times 10^{-5}$ Ω cm, $5.027(7) \times 10^{-4}$ Ω cm, and 220.1(1) K, respectively. The result indicates that the dominant scattering mechanism is electron–phonon intraband scattering, as expected for materials that are not *s* or *sp* metals.[35,53,54]

The upturn in resistivity on cooling at low temperatures can be explained by

$$\rho'(T) = \rho_0' - m_p'\sqrt{T} + (BT^2 - C_1T^{5/2}) + \mathrm{BG} \quad (2)$$

where the ρ_0 is the residual resistivity obtained in high-temperature fits, the second term arises from the Coulomb-enhanced electron–electron interaction in disordered systems, the third term denotes the contribution of the strength of diffusive spin excitation, and the BG term depicts the scattering of conduction electrons by phonons.[55−57] The $\rho(T)$ curve below 15 K can be well fitted by using eq 2 (Figure 2h inset). This is similar to NiMnSn and CuMn magnetic glass alloys.[35,58,59] The fitting parameters ρ_0', m_p', B, C_1, C', and Θ_D' are $4.1(3) \times 10^{-5}$ Ω cm, $1.79(2) \times 10^{-6}$ Ω cm $K^{-1/2}$, $11(1) \times 10^{-9}$ Ω cm K^{-2}, $8(2) \times 10^{-10}$ Ω cm $K^{-5/2}$, $5.0(1) \times 10^{-4}$ Ω cm, and 220.1(1) K, respectively. When compared to NiMnSn and CuMn alloys, the $\sim\sqrt{T}$ is about 1 order of magnitude higher, implying stronger electron–electron interaction effects, similar to that of $Fe_{0.33}Pd_{0.67}Se_2$.[35]

At high temperatures (Figure 2i), heat capacity approaches the Dulong–Petit value of $3NR = 74.8(3)$ J mol^{-1} K^{-1}. Due to the large atom mass difference between Fe and Pd atoms, in the full temperature range, heat capacity can be fitted using the double-Debye model along with a spin-glass term.[35,60,61] The total specific heat then becomes[60,62]

https://doi.org/10.1021/acs.inorgchem.5c02764
Inorg. Chem. 2025, 64, 23825−23833

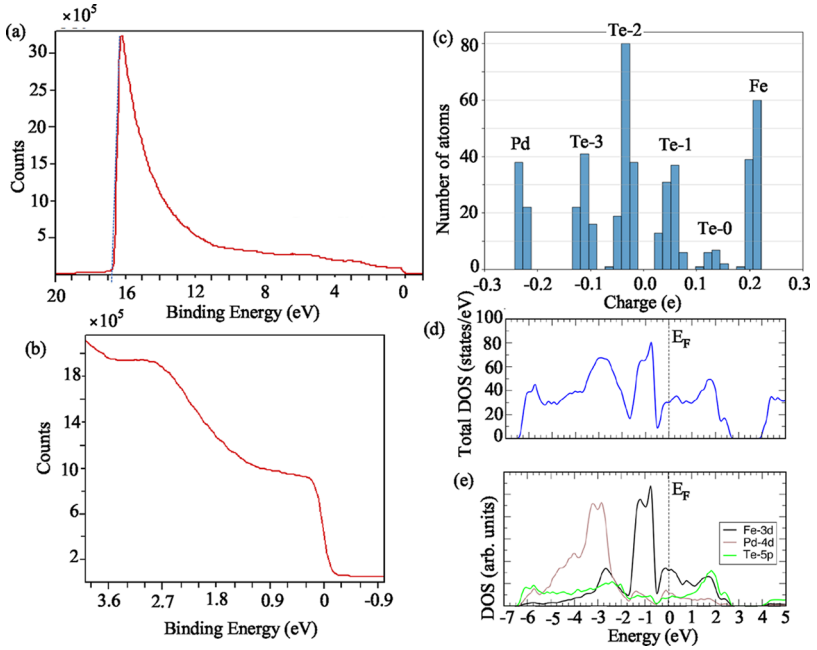

Figure 4. (a,b) UPS spectra for $Fe_{0.6(1)}Pd_{0.4(1)}Te_2$ at room temperature and energy range near the Fermi level. (c) Distribution of atomic charges in $Fe_{0.625}Pd_{0.375}Te_2$ calculated by DFT. The bars showing the count of different atomic species are labeled according to the notation from the main text. Total (d) and (e) atom-projected densities of states of $Fe_{0.625}Pd_{0.375}Te_2$.

$$C_P(T) = MT^2 + \gamma T + 9R(N - s)\left(\frac{T}{\Theta_{D1}}\right)^3 \int_0^{\Theta_{D1}/T} \frac{x^4 e^x}{(e^x - 1)^2} dx + 9Rs\left(\frac{T}{\Theta_{D2}}\right)^3 \int_0^{\Theta_{D2}/T} \frac{x^4 e^x}{(e^x - 1)^2} dx \quad (3)$$

where Θ_{D1} and Θ_{D2} are the Debye temperatures for each sublattice, s is the number of oscillators in one sublattice, set to a fitting parameter, and MT^2 is the spin glass contribution.[61] We obtained the Debye temperatures by assuming $N = 3$; fit yields $s = 1.03(7)-1$, hence there are 2 oscillators in one lattice and 1 in the other ($N = 3$, $s = 1$).[62] The acquired Θ_{D1}, Θ_{D2}, M, and γ are 287(3) K, 165(3) K, $4.34(1) \times 10^{-16}$ mJ mol^{-1} K^{-3}, and 7.5(2) mJ mol^{-1} K^{-2}, respectively. The obtained Debye temperatures Θ_{D1} and Θ_{D2} are relatively close to the ones obtained resistivity fits (Figure 2h). This could indicate that high-temperature phonon scattering involves both sublattices. The Debye temperature Θ_D is smaller than that of of pyrite $Fe_{0.33}Pd_{0.67}Se_2$[35] but is similar to KNi_2Se_2.[60]

The Wilson ratio $R_W = \pi^2 k_B^2 \chi / 3\ \mu_B^2 \gamma$, where χ is the magnetic susceptibility, γ is the electronic heat capacity, k_B and μ_B are the Boltzmann constant and Bohr magneton, respectively, is a dimensionless quantity of the order of unity for noninteracting systems, whereas it takes a value of 2 for strongly interacting Kondo systems such as for the $S = 1/2$ Kondo model.[63,64] From $\gamma = 7.8(9)$ mJ mol^{-1} K^{-2} and $\chi = 0.000185(5)$ emu mol^{-1} Oe^{-1}, we obtain $R_W = 1.71(3)$. This is comparable to LiV_2O_4, suggesting the presence of strong electronic correlations.[65]

XPS and UPS Properties. XPS spectra of $Fe_{0.6}Pd_{0.4}Te_2$ taken at room temperature are presented in Figure 3a–f, with Fe, Pd, and Te spectra shown in a,d; b,e; and c,f; respectively. Data taken before (after) Ar^+ sputtering are presented in a–c (d–f). Before Ar^+ sputtering, the XPS shows that all of the Fe, Pd, and Te in the surface region, less than 10 nm, are partially oxidized. In the Fe 2p spectrum (Figure 3a), the peaks at 706.4 and 719.5 eV correspond to Fe $2p_{3/2}$ and Fe $2p_{1/2}$, respectively, indicating the presence of metallic itinerant Fe states (Fe^0). An additional doublet of peaks attributed to Fe_2O_3 (Fe^{3+}) was observed at higher binding energies of 710.9 and 724.5 eV due to prolonged exposure of the crystal to the air.[66−68] Although the Pd spectrum shows a negligible difference before and after Ar^+ sputtering (Figure 3b,e), in the Te 3d spectrum (Figure 3c), peaks at 572.6 and 583.0 eV correspond to Te $3d_{5/2}$ and Te $3d_{3/2}$, which are associated with the metallic Te (Te^0) zero valence state. In addition, the doublet attributed to TeO_2 (Te^{4+}) oxide was observed at 576.0 and 586.4 eV.[66,67]

The peak positions and shape of the Fe2p and Te3d observed here are in line with those of the $FeTe_2$ crystals with 10% Fe vacancies.[25] In the Pd 3d spectrum (Figure 3b), the peaks at 336.2 and 341.5 eV correspond to Pd $3d_{5/2}$ and Pd $3d_{3/2}$. The Pd $3d_{5/2}$ values for metallic Pd and PdO were reported in the range of 334.8−335.4 and 336.3−336.8 eV,[69,70] respectively. Therefore, the observation suggests a mixture of the metallic Pd valence state and PdO in the surface region.

To identify the chemical state of each element in bulk, the sample surface was Ar^+-sputtered in order to remove the oxidized surface layers. The XPS in Figure 3d–f shows that all of the Fe, Pd, and Te are in metallic states in bulk without oxidized states as evidenced by the absence of oxidized doublets of Fe 2p and Te 3d as well as the 0.6 eV shift of Pd 3d toward lower binding energies. In details, the doublet peaks of Fe $2p_{3/2}$ and Fe $2p_{1/2}$ at 706.5 and 719.6 eV correspond well to 706.7 eV binding energy for metallic Fe $2p_{1/2}$, as well as to the overall spectral shape.[66−68] Compared to the typical metallic state of Te $3d_{5/2}$ in the range of binding energies of 572.7−572.9 eV,[66−68] the doublet Te $3d_{5/2}$ and Te $3d_{3/2}$ at 572.4 and 582.8 eV are slightly shifted, about −0.3 eV to −0.5 eV to lower binding energy. Compared to the typical metallic state of Pd $3d_{5/2}$ in the range of 334.8−335.4 eV,[69,71] the doublets Pd $3d_{5/2}$ and Pd $3d_{3/2}$ at 335.6 and 340.9 eV are slightly shifted by

https://doi.org/10.1021/acs.inorgchem.5c02764
Inorg. Chem. 2025, 64, 23825−23833

+0.2 to +0.8 eV to higher binding energy. The above observations suggest that the electropositive Pd cations are surrounded by an electronegative Te atom as expected (Figure 1b). This is consistent with larger electron affinities of Te when compared to Pd.

The UPS spectrum is depicted in Figure 4a. As depicted in Figure 4b, the UPS shows the metallic nature at room temperature, as evidenced by the density of state (DOS) curve across the Fermi level. The secondary electron emission cutoff at 16.7 eV, resulting from UV irradiation with a photo energy of 21.2 eV, indicates that the work function is about 4.5 eV, which is within the range of the theoretically predicted work functions for $FeTe_2$ (4.23 eV) and FeTeS (4.65 eV).[72]

Although Te atomic vacancy defects do not change the unit cell symmetry in marcasite $FeTe_2$, we note that metal deficiency in $IrTe_2$ induces a pyrite structure via the reinforcement of Te−Te bonds via charge decrease caused by electron depletion in Te−Te antibonding states, thus leading to Te_2 pairs.[25,73] There is no evidence for metal vacancies when Pd is substituted on the Fe atomic site in $Fe_{0.6}Pd_{0.4}Te_2$ (Figure 1 and Table 1). Therefore, Te pairs are likely induced by a somewhat larger covalent radius of Pd. The possible mechanism includes a steric effect where Te atoms are pushed apart by larger Pd favoring more symmetric packing or changes in directional covalent preferences induced by larger Pd atoms as in rock salt GeTe alloyed with Sn on the Ge atomic site.[74,75] Finally, increased and more delocalized valence electron count could also lead to a higher unit cell symmetry due to covalent bond disruption in the parent structure.[76] Pyrite-type $FeTe_2$ synthesized at high pressure is a semimetal, suggesting an increase in conductivity when compared to marcasite-type $FeTe_2$.[10] Therefore, the metallic state in our sample should be induced by both the higher unit cell symmetry of the pyrite structure and the increased electron count and orbital delocalization brought about by Pd atoms.

Electronic Structure. Our DFT calculations reveal no evidence of Pd-induced charge localization at the Te_2 dimers, ruling this mechanism out as the origin of the observed core-level shift in Te. However, Bader charge analysis presents a distinct perspective. Both Fe and Pd atoms exhibit 6-fold coordination with Te nearest neighbors, with calculated Bader charges of +0.21(1) and −0.23(1), respectively. Each Te atom is coordinated with three transition-metal atoms (Fe or Pd) and one Te atom. The Bader charge analysis reveals a systematic dependence of the Te charge on its local coordination environment, which can be classified into four distinct categories based on the number of Fe nearest neighbors (NNs): (i) Te-3: Te atoms coordinated with three Fe NNs exhibit a charge of −0.11(2)e, (ii) Te-2: Te atoms with two Fe and one Pd NN carry a charge of −0.03(2)e, (iii) Te-1: Te atoms bonded to one Fe and two Pd NNs show a charge of +0.05(2)e, and (iv) Te-0: Te atoms surrounded exclusively by three Pd NNs possess a charge of +0.13(2)e.

In contrast, the charges on Fe and Pd atoms remain nearly constant at +0.21e and −0.23e, respectively, with minimal variation (±0.01e). This consistency reflects their stable local environments, at least when only nearest-neighbor interactions are considered. The histogram (Figure 4c) identifies the common charges in the system. We note a large Pauling electronegativity difference between Pd (2.20) and Fe (1.83). This drives a partial electron depletion from Te atoms when Pd replaces Fe in their coordination environment, as evidenced by our Bader charge analysis, since Te charges become progressively less negative with increasing Pd neighbors. Thus, the dominant electronic effect stems from the Fe/Pd substitution, rather than the absolute electronegativity ranking of Pd and Te. The metallic character of the system, as evidenced by the UPS spectrum, is further supported by our DFT calculations (Figure 4d). A detailed examination of the electronic states near the Fermi level reveals their hybridized nature. As shown in the atom-projected density of states (DOS) in Figure 4e, all three constituent elements contribute to states at the Fermi level, with significant Fe 3*d*, Pd 4*d*, and Te 5*p* orbital contributions.

In $Fe_{0.6(1)}Pd_{0.4(1)}Te_2$, each Pd atom with Pauling electronegativity $\chi_P = 2.20$ is coordinated by six Te atoms ($\chi_P = 2.10$), while each Te is coordinated by three transition metals, Fe ($\chi_P = 1.83$), or Pd, thus creating an asymmetry in coordination number. Although Pd is slightly more electronegative than Te, its per-bond effective electronegativity is diluted across six Pd−Te bonds (about 0.37 per bond), whereas each Te turns into a relatively higher per-bond electronegativity (0.70 per bond), so Pd 4*d* electrons shift toward Te (away from Pd) along the Pd−Te bonds. The intrinsic delocalized nature of 4*d* orbitals overlaps with that of Te 5*p* orbitals in each Pd−Te bond, expanding the integrated electron volume associated with Pd and resulting in a total negative Bader charge (−0.23), enhanced by Te 5*p* contributions in a relatively large Bader volume compared to metallic Pd. Meanwhile, since the local electron density of Pd 4*d* orbitals redistributes toward Te and away from the Pd core as well as is symmetrically diluted across six Pd−Te bonds, the screening of the Pd core levels is weakened. This reduced screening shifts the Pd 3*d* levels to higher binding energy in XPS. Fe exhibits a positive Bader charge (+0.21) due to partial transfer of Fe 3*d* electrons to neighboring Te because of its relative lower electronegativity, but its itinerant delocalized 3*d* electrons maintain the metallic Fe state. Te gains electrons mainly from Fe, producing a negative Bader charge (−0.11); the increased local density near the Te nucleus efficiently screens its core, resulting in a reduced Te chemical state. Thus, coordination numbers, per-bond electronegativity differences, and the delocalized nature of *d* orbitals influence the spatial distribution of valence electrons and, thereby, govern the chemical states observed by XPS.

Bader charge analysis provides valuable insight into the valence electron density redistribution for understanding chemical states, but it does not always correlate directly with the chemical states observed by XPS.[77−79] Our combined DFT and XPS study shows that chemical states are governed not only by the total Bader charge but also by local coordination, spatial charge distribution, and hence initial-state screening effects. Thus, Bader analysis and XPS offer complementary perspectives for a comprehensive characterization of the electronic structure and chemical states, as demonstrated here.

CONCLUSIONS

In summary, we report the synthesis of the high-pressure pyrite polymorph of $FeTe_2$ using Pd substitution on the Fe atomic site using an ambient pressure synthesis method. The pyrite $Fe_{0.6(1)}Pd_{0.4(1)}Te_2$ is a paramagnetic metal with a possible disorder-induced scattering of correlated electronic states at low temperatures, arising from magnetic spin glass and diffusive spin fluctuations. Further interest would be to test the catalytic properties of this material.

https://doi.org/10.1021/acs.inorgchem.5c02764
Inorg. Chem. 2025, 64, 23825−23833

■ ASSOCIATED CONTENT

Accession Codes

Deposition Number 2473324 contains the supplementary crystallographic data for this paper. These data can be obtained free of charge via the joint Cambridge Crystallographic Data Centre (CCDC) and Fachinformationszentrum Karlsruhe Access Structures service.

■ AUTHOR INFORMATION

Corresponding Authors

Cedomir Petrovic − *Shanghai Key Laboratory of Material Frontiers Research in Extreme Environments (MFree), Shanghai Advanced Research in Physical Sciences (SHARPS), Shanghai 201203, China; Center for High Pressure Science and Technology Advanced Research (HPSTAR), 201203 Shanghai, China; SHARPS - Republic of Serbia, Vinca Institute of Nuclear Sciences, University of Belgrade, Belgrade 11001, Serbia; Condensed Matter Physics and Materials Science Department, Brookhaven National Laboratory, Upton, New York 11973, United States;* orcid.org/0000-0001-6063-1881; Email: cedomir.petrovic@sharps.ac.cn

Jianjun Tian − *Henan Key Laboratory of Quantum Materials and Quantum Energy, School of Quantum Information Future Technology, Henan University, Kaifeng 475004, China;* orcid.org/0000-0002-1630-1671; Email: tjj@henu.edu

Xiao Tong − *Center of Functional Nanomaterials, Brookhaven National Laboratory, Upton, New York 11973, United States*; Email: xtong@bnl.gov

Authors

Wanping Wang − *Henan Key Laboratory of Quantum Materials and Quantum Energy, School of Quantum Information Future Technology, Henan University, Kaifeng 475004, China; Center for High Pressure Science and Technology Advanced Research (HPSTAR), 201203 Shanghai, China*

Michael O. Ogunbunmi − *Department of Chemistry and Biochemistry, University of Delaware, Newark, Delaware 19716, United States; Department of Physics and Engineering, Xavier University of Louisiana, New Orleans, Louisiana 70125, United States;* orcid.org/0000-0002-5340-9198

Yang Fu − *Center for High Pressure Science and Technology Advanced Research (HPSTAR), 201203 Shanghai, China*

Zhixiang Hu − *Center for High Pressure Science and Technology Advanced Research (HPSTAR), 201203 Shanghai, China*

Svilen Bobev − *Department of Chemistry and Biochemistry, University of Delaware, Newark, Delaware 19716, United States;* orcid.org/0000-0002-0780-4787

Zeljko Sljivancanin − *Vinca Institute of Nuclear Sciences, University of Belgrade, Belgrade 11001, Serbia;* orcid.org/0000-0001-8575-2575

Hechang Lei − *School of Physics and Beijing Key Laboratory of Optoelectronic Functional Materials and Micro-Nano Devices and Key Laboratory of Quantum State Construction and Manipulation (Ministry of Education), Renmin University of China, Beijing 100872, China*

Weifeng Zhang − *Henan Key Laboratory of Quantum Materials and Quantum Energy, School of Quantum Information Future Technology, Henan University, Kaifeng 475004, China*

Complete contact information is available at: https://pubs.acs.org/10.1021/acs.inorgchem.5c02764

Notes

The authors declare no competing financial interest.

■ ACKNOWLEDGMENTS

C.P. acknowledges financial support from the Shanghai Key Laboratory of Novel Extreme Condition Materials, China (no. 22dz2260800), and the Shanghai Science and Technology Committee, China (no. 22JC1410300). Work at the Brookhaven National Laboratory was supported by US DOE, Office of Science, Office of Basic Energy Sciences, under contract DE-SC0012704. The work carried out at the University of Delaware was supported by the U.S. Department of Energy, Office of Science, Basic Energy Sciences, under Award DE-SC0008885. This research used the resources of the Center for Functional Nanomaterials, which is a U.S. Department of Energy Office of Science User Facility, at BNL under Contract No. DE-SC0012704. H.L. was supported by the National Key R&D Program of China (Grants Nos. 2023YFA1406500 and 2022YFA1403800) and the National Natural Science Foundation of China (Grant No. 12274459). Work at the Vinca Institute was funded by the Ministry of Science, Technological Development, and Innovation of the Republic of Serbia via project 0112507.

■ REFERENCES

(1) de la Barrera, S. C.; Sinko, M. R.; Gopalan, D. P.; Sivadas, N.; Seyler, K. L.; Watanabe, K.; Taniguchi, T.; Tsen, A. W.; Xu, X.; Xiao, D.; Hunt, B. M. Tuning Ising superconductivity with layer and spin-orbit coupling in two-dimensional transition metal dichalcogenides. *Nat. Commun.* **2018**, *9*, 1427.

(2) Xing, Y.; Yang, P.; Ge, J.; Yan, J.; Luo, J.; Ji, H.; Yang, Z.; Li, Y.; Wang, Z.; Liu, Y.; Yang, F.; Qiu, P.; Xi, C.; Tian, M.; Liu, Y.; Lin, X.; Wang, J. Extrinsic and intrinsic anomalous metallic states in transition metal dichalcogenide Ising superconductors. *Nano Lett.* **2021**, *21*, 7486−7494.

(3) Yang, J. J.; Choi, Y. J.; Oh, Y. S.; Hogan, A.; Horibe, Y.; Kim, K.; Min, B. I.; Cheong, S. W. Charge-orbital density wave and superconductivity in the strong spin-orbit coupled $IrTe_2$:Pd. *Phys. Rev. Lett.* **2012**, *108*, No. 116402.

(4) Sipos, B.; Kusmartseva, A. F.; Akrap, A.; Berger, H.; Forró, L.; Tutiš, E. From Mott state to superconductivity in 1T-TaS_2. *Nat. Mater.* **2008**, *7*, 960−965.

(5) Yu, Y.; Yang, F.; Lu, X. F.; Yan, Y. J.; Cho, Y.-H.; Ma, L.; Niu, X.; Kim, S.; Son, Y.-W.; Feng, D.; Li, S.; Cheong, S.-W.; Chen, X. H.; Zhang, Y. Gate-tunable phase transitions in thin flakes of 1T-TaS_2. *Nat. Nanotechnol.* **2015**, *10*, 270−276.

(6) Xu, Z.; Yang, H.; Song, X.; Chen, Y.; Yang, H.; Liu, M.; Huang, Z.; Zhang, Q.; Sun, J.; Liu, L.; Wang, Y. Topical review: recent progress of charge density waves in 2D transition metal dichalcogenide-based heterojunctions and their applications. *Nanotechnology* **2021**, *32*, 492001.

(7) Luo, H.; Krizan, W.; Seibel, E. M.; Xie, W.; Sahasrabudhe, G. S.; Bergman, S. L.; Phelan, B. F.; Tao, J.; Wang, Z.; Zhang, J.; Cava, R. J. Cr-Doped $TiSe_2$ A layered dichalcogenide spin glass. *Chem. Mater.* **2015**, *27*, 6810−6817.

(8) Grønvold, F.; Røst, E. On the Sulfides, Selenides and Tellurides of Palladium. *Acta Chem. Scand.* **1956**, *10*, 1620−1634.

(9) Tengner, S. Uber Diselenide und Ditelluride von Eisen, Kobalt und Nickel. *Z. Anorg. Allg. Chem.* **1938**, *239*, 126−132.

(10) Bither, T. A.; Bouchard, R. J.; Cloud, W. H.; Donohue, P. C.; Siemens, W. J. Transition metal pyrite dichalcogenides. High-pressure synthesis and correlation of properties. *Inorg. Chem.* **1968**, *7*, 2208−2220.
(11) Raub, Ch. J.; Compton, V. B.; Geballe, T. H.; Matthias, B. T.; Maita, J. P.; Hull, G. W. The occurrence of superconductivity in sulfides, selenides, tellurides of Pt-group metals. *J. Phys. Chem. Solids* **1965**, *26*, 2051−2057.
(12) Liu, Y.; Zhao, J. Z.; Yu, L.; Lin, C. T.; Liang, A. J.; Hu, C.; Ding, Y.; Xu, Y.; He, S. L.; Zhao, L.; Liu, G. D.; Dong, X. L.; Zhang, J.; Chen, C. T.; Xu, Z. Y.; Weng, H. M.; Dai, X.; Fang, Z.; Zhou, X. J. Identification of topological surface state in $PdTe_2$ superconductor by angle-resolved photoemission spectroscopy. *Chin. Phys. Lett.* **2015**, *32*, No. 067303.
(13) Teknowijoyo, S.; Jo, N. H.; Scheurer, M. S.; Tanatar, M. A.; Cho, K.; Bud'ko, S. L.; Orth, P. P.; Canfield, P. C.; Prozorov, R. Nodeless superconductivity in the type-II Dirac semimetal $PdTe_2$: London penetration depth and pairing-symmetry analysis. *Phys. Rev. B* **2018**, *98*, No. 024508.
(14) Clark, O. J.; Neat, M. J.; Okawa, K.; Bawden, L.; Markovic, I.; Mazzola, F.; Feng, J.; Sunko, V.; Riley, J. M.; Meevasana, W.; Fujiii, W.; Vobornik, I.; Kim, T. K.; Hoesch, M.; Sasagawa, T.; Wahl, P.; Bahramy, M. S.; King, P. D. C. Fermiology and Superconductivity of Topological Surface States in $PdTe_2$. *Phys. Rev. Lett.* **2018**, *120*, No. 156401.
(15) Pelayo, I.; Bergner, D.; Williams, A. J.; Qi, J.; Zhu, P.; Nabi, M.; Huey, W. L. B.; Moreschini, L.; Deng, Z.; Hadsell, T.; Denlinger, J.; Lanzara, A.; Lu, Y. M.; Windl, W.; Goldberger, J.; Ojeda-Aristizabal, C. Three-dimensional dispersion in the type-II Dirac semimetals $PtTe_2$ and $PdTe_2$ revealed through circular dichroism in angle-resolved photoemission spectroscopy. *Phys. Rev. B* **2024**, *110*, No. 195429.
(16) Noh, H. J.; Jeong, J.; Cho, E. J.; Kim, K.; Min, B. I.; Park, B. G. Experimental realization of Type-II Dirac Fermions in a $PdTe_2$ superconductor. *Phys. Rev. Lett.* **2017**, *119*, No. 016401.
(17) Fei, F.; Bo, X.; Wang, R.; Wu, B.; Jiang, J.; Fu, D.; Gao, M.; Zheng, H.; Chen, Y.; Wang, X.; Bu, H.; Song, F.; Wan, X.; Wang, B.; Wang, G. Nontrivial Berry phase and type-II Dirac transport in the layered material $PdTe_2$. *Phys. Rev. B* **2017**, *96*, No. 041201.
(18) Xiao, R. C.; Gong, P. L.; Wu, Q. S.; Lu, W. J.; Wei, M. J.; Li, J. Y.; Lv, H. Y.; Luo, X.; Tong, P.; Zhu, X. B.; Sun, Y. P. Manipulation of type-I and type-II Dirac points in $PdTe_2$ superconductor by external pressure *Phys. Rev. B* **2017**, *96*, No. 075101.
(19) D'Olimpio, G.; Guo, C.; Kuo, C.; Edla, R.; Lue, C. S.; Ottaviano, L.; Torelli, P.; Wang, L.; Boukhvalov, D. W.; Politano, A. $PdTe_2$ Transition-Metal Dichalcogenide: Chemical Reactivity, Thermal Stability, and Device Implementation. *Adv. Funct. Mater.* **2020**, *30*, No. 1906556.
(20) Guo, Y.; Chen, Z.; Jin, Z.; Wang, X.; Zhang, C.; Balakin, A. V.; Shkurinov, A. P.; Peng, Y.; Zhu, Y.; Zhuang, S. Dynamically Controllable Terahertz Electromagnetic Interference Shielding by Small Polaron Responses in Dirac Semimetal $PdTe_2$ Thin Films. *Adv. Funct. Mater.* **2024**, *34*, No. 2407749.
(21) Zeng, L.; Han, W.; Ren, X.; Li, X.; Wu, D.; Liu, S.; Wang, H.; Lau, S. P.; Tsang, Y. H.; Shan, C. X.; Jie, J. Uncooled Mid-Infrared Sensing Enabled by Chip-Integrated Low-Temperature-Grown 2D $PdTe_2$ Dirac Semimetal. *Nano Lett.* **2023**, *23*, 8241.
(22) Zhang, L.; Guo, C.; Kuo, C. N.; Xu, H.; Zhang, K.; Ghosh, B.; De Santis, J.; Boukhvalov, D. W.; Vobornik, I.; Paolucci, V.; Lue, C. S.; Xing, H.; Agarwal, A.; Wang, L.; Politano, A. Terahertz Photodetection with Type-II Dirac Fermions in Transition-Metal Ditellurides and Their Heterostructures. *Phys. Status Solidi RRL* **2021**, *15*, No. 2100212.
(23) He, Y.; Yan, D.; Wang, S.; Shi, L.; Zhang, X.; Yan, K.; Luo, H. Topological Type-II Dirac Semimetal and Superconductor $PdTe_2$ for Ethanol Electrooxidation. *Energy Technol.* **2019**, *7*, No. 1900663.
(24) Zuo, Y.; Antonatos, N.; Dêkanovský, L.; Luxa, J.; Elliott, J. D.; Gianolio, D.; Šturala, J.; Guzzetta, F.; Mourdikoudis, S.; Regner, J.; Málek, R.; Sofer, Z. Defect Engineering in Two-Dimensional Layered PdTe2 for Enhanced Hydrogen Evolution Reaction. *ACS Catal.* **2023**, *13*, 2601.
(25) Tian, J.; Ivanovski, V. N.; Abeykoon, M.; Martin, R. M.; Baranets, S.; Martin, C.; Liu, Y.; Du, Q.; Wang, A.; Chen, S.; Tong, X.; Zhang, W.; Bobev, S.; Koteski, V.; Petrovic, C. Absence of long-range magnetic order in $Fe_{1-\delta}Te_2$ ($\delta \approx 0.1$) crystals. *Phys. Rev. B* **2021**, *104*, No. 224109.
(26) Rahman, A.; Zhang, D.; Rehman, M. U.; Zhang, M.; Wang, X.; Dai, R.; Wang, Z.; Tao, X.; Zhang, Z. Multiple magnetic phase transitions, electrical and optical properties of $FeTe_2$ single crystals. *J. Phys.: Condens. Matter* **2020**, *32*, No. 035808.
(27) Yang, L.; Liu, J.; Liu, Y.; Li, Y.; Zuo, F.; Wu, Y.; Li, Q.; Li, H. Long life exceeding 10 000 cycles for aluminumion batteries based on an $FeTe_2$@GO composite as the cathode. *Chem. Commun.* **2022**, *58*, 10981.
(28) Duraivel, M.; Nagappan, S.; Mohanraj, K.; Prabakar, K. Pyrite copper nickel sulfide for stable hydrogen evolution reaction in alkaline media. *Int. J. Hydrogen Energy* **2024**, *54*, 1040.
(29) Mukherjee, A.; Subedi, A. Thermoelectric Transport Properties of Electron-Doped Pyrite FeS_2. *J. Phys. Chem. C* **2024**, *128*, 6573.
(30) Yang, C.; Yue, J.; Wang, G.; Luo, W. Activating and Identifying the Active Site of RuS2 for Alkaline Hydrogen Oxidation Electrocatalysis. *Angew. Chem.* **2024**, *136*, No. e202401453.
(31) Matsumura, M.; Endoh, Y.; Hiraka, H.; Yamada, K.; Mischenko, A. S.; Nagaosa, N.; Solovyev, I. V. Classical and quantum spin dynamics in the fcc antiferromagnet NiS_2 with frustration. *Phys. Rev. B* **2003**, *68*, No. 094409.
(32) Timirgazin, M. A.; Igoshev, P. A.; Arzhinikov, A. K.; Irkhin, Yu. Magnetic states, correlation effects and metal-insulator transition in FCC lattice. *J. Phys.: Condens. Matter* **2016**, *28*, No. 505601.
(33) Kimber, S. A. J.; Chatterji, T. Spin-driven symmetry breaking in the frustrated fcc pyrite MnS_2. *J. Phys.: Condens. Matter* **2015**, *27*, No. 226003.
(34) Diep, H. T.; Ghazali, A.; Berge, B.; Lallemand, P. Phase Diagrams in f.c.c. Binary Alloys: Frustration Effects. *Europhys. Lett.* **1986**, *2*, 603.
(35) Tian, J.; Ivanovski, V. N.; Szalda, D.; Lei, H.; Wang, A.; Liu, Y.; Zhang, W.; Koteski, V.; Petrovic, C. $Fe_{0.36(4)}Pd_{0.64(4)}Se_2$: Magnetic spin-glass polymorph of $FeSe_2$ and $PdSe_2$ stable at ambient pressure. *Inorg. Chem.* **2019**, *58*, 3107−3114.
(36) Fisk, Z.; Remeika, J. P. Growth of single crystals from molten metallic fluxes. In *Handbook on the Physics and Chemistry of Rare Earths*; Gschneidner, K. A.; Eyring, L., Eds.; Elsevier: Amsterdam, 1989; Vol. *12*, p 53.
(37) Canfield, P.; Fisk, Z. Growth of single crystals from metallic fluxes. *Philos. Mag. B* **1992**, *65*, 1117.
(38) Canfield, P. C.; Fisher, I. High-temperature solution growth of intermetallic single crystals and quasicrystals. *J. Cryst. Growth* **2001**, *225*, 155.
(39) Kanatzidis, M. G.; Pottgen, R.; Jeitschko, W. The metal flux: a preparative tool for the exploration of intermetallic compounds. *Angew. Chem. Int. Ed.* **2005**, *44*, 6996.
(40) Hunter, G. RIETICA, A Visual Rietveld Program. *International Union of Crystallography Commission on Powder Diffraction Newsletter* **1998**, *20*, 16.
(41) Sheldrick, G. M. Crystal structure refinement with SHELXL. *Acta Crystallogr. C* **2015**, *71*, 3.
(42) *International Tables for Crystallography, Vol. C*, 6th ed.; Wilson, A. J. C.; Prince, E., Eds.; Kluwer Academic Publishers: Norwell, MA, 1999; p 548.
(43) Enkovaara, J.; Rostgaard, C.; Mortensen, J. J.; Chen, J.; Dułak, M.; Ferrighi, L.; Gavnholt, J.; Glinsvad, C.; Haikola, V.; Hansen, H. A.; Kristoffersen, H. H.; Kuisma, M.; Larsen, A. H.; Lehtovaara, L.; Ljungberg, M.; Lopez-Acevedo, O.; Moses, P. G.; Ojanen, J.; Olsen, T.; Petzold, V.; Romero, N. A.; Stausholm-Møller, J.; Strange, M.; Tritsaris, G. A.; Vanin, M.; Walter, M.; Hammer, B.; Häkkinen, H.; Madsen, G. H. K.; Nieminen, R. M.; Nørskov, J. K.; Puska, M.; Rantala, T. T.; Schiøtz, J.; Thygesen, K. S.; Jacobsen, K. W. Electronic structure calculations with GPAW: a real space implementation of the

https://doi.org/10.1021/acs.inorgchem.5c02764
Inorg. Chem. 2025, 64, 23825−23833

projector augmented-wave method. *J. Phys.: Condens. Matter* **2010**, *22*, No. 253202.
(44) Liu, D. C.; Nocedal, J. On the Limited Memory Method for Large Scale Optimization. *Math. Program.* **1989**, *45*, 503.
(45) Blöchl, P. E. Projector augmented-wave method. *Phys. Rev. B* **1994**, *50*, 17953.
(46) Mortensen, J.; Hansen, L. B.; Jacobsen, K. W. Real-space grid implementation of the projector augmented wave method. *Phys. Rev. B* **2005**, *71*, No. 035109.
(47) Perdew, P.; Burke, K.; Ernzerhof, M. Generalized Gradient Approximation Made Simple. *Phys. Rev. B* **1996**, *77*, 3865.
(48) Monkhorst, H. J.; Pack, J. D. Special points for Brillouin-zone integrations. *Phys. Rev. B* **1976**, *13*, 5188.
(49) Bader, R. F. W. *Atoms in Molecules: A Quantum Theory*; Oxford University Press: New York, 1990.
(50) Korenstein, R.; Henry, R. L.; Wold, A. High-pressure phase transformations of the systems $Ni_{1-x}Co_xTe_2$ and $Ni_{1-x}Fe_xTe_2$. *Inor. Chem.* **1976**, *15*, 3031−3034.
(51) Mydosh, J. A. *Spin Glasses: An Experimental Introduction*; Taylor & Francis: London, 1993.
(52) Chu, D.; Kenning, G. G.; Orbach, R. Dynamic measurements in a Heisenberg spin glass: CuMn. *Phys. Rev. Lett.* **1994**, *72*, 3270−3273.
(53) Blatt, F. J. *Physics of Electronic Conduction in Solids*; McGraw-Hill: New York, 1968.
(54) Goetsch, R. J.; Anand, V. K.; Pandey, A.; Johnston, D. C. Structural, thermal, magnetic, and electronic transport properties of the $LaNi_2(Ge_{1-x}P_x)_2$ system. *Phys. Rev. B* **2012**, *85*, No. 054517.
(55) Lee, P. A.; Ramakrishnan, T. V. Disordered electronic systems. *Rev. Mod. Phys.* **1985**, *57*, 287−337.
(56) Fischer, K. H. On the electrical resistivity of spin glasses. *Z. Phys. B* **1979**, *34*, 45−53.
(57) Altshuler, B. L.; Aronov, A. G.*Electron-Electron Interactions in Disordered Systems*; Efros, A. L.; Pollak, M., Eds.; Elsevier: Amsterdam, 1985.
(58) Singh, S.; Pal, S.; Biswas, C. Disorder iduced resistivity anomaly in $NiMn_{1+x}Sn_{1-x}$. *J. Alloys Compd.* **2014**, *616*, 110−115.
(59) Chakraborty, S.; Majumdar, A. K. Resistivity minima in concentrated γ-$Cu_{100-x}Mn_x$ alloys ($36 \leq x \leq 83$). *Phys. Rev. B* **1996**, *53*, 6235−6239.
(60) Lei, H.; Abeykoon, M.; Wang, K.; Bozin, E. S.; Ryu, H.; Graf, D.; Warren, J. B.; Petrovic, C. Physical properties of $K_xNi_{2-x}Se_2$ single crystals. *J. Phys.: Conden. Matter* **2014**, *26*, No. 015701.
(61) Fogle, W.; Ho, J. C.; Philipps, N. E. Concentration and temperature dependence of the magnetic heat capacity of dilute $CuMn_x$. *J. Phys. Colloq.* **1978**, *39*, C6-901−C6-902.
(62) Neilson, J. R.; Llobet, A.; Stier, A. V.; Wu, L.; Wen, J.; Tao, J.; Zhu, Y.; Tesanovic, Z. B.; Armitage, N. P.; McQueen, T. M. Mixed-valence-driven heavy-fermion behavior and superconductivity in KNi_2Se_2. *Phys. Rev. B* **2012**, *86*, No. 054512.
(63) Hewson, A. C. *The Kondo Problem to Heavy Fermions, Cambridge Studies in Magnetism*; Cambridge University Press: 1993.
(64) Stewart, G. Heavy Fermion Systems. *Rev. Mod. Phys.* **1984**, *86*, 755−787.
(65) Kondo, S.; Johnston, D. C.; Swenson, C. A.; Borsa, F.; Mahajan, A. V.; Miller, L. L.; Gu, T.; Goldman, A. I.; Maple, B. M.; Gajewski, D. A.; Freeman, E. J.; Dilley, N. R.; Dickey, R. P.; Merrin, J.; Kojima, K.; Luke, G. M.; Uemura, Y. J.; Chmaissem, O.; Jorgensen, J. D. LiV_2O_4: A Heavy Fermion Transition Metal Oxide. *Phys. Rev. Lett.* **1997**, *78*, 3729−3732.
(66) Telesca, D.; Nie, Y.; Budnick, J. I.; Wells, B. O.; Sinkovic, B. Surface valence states and stoichiometry of non-superconducting and superconducting FeTe films. *Surf. Sci.* **2012**, *606*, 1056.
(67) Telesca, D.; Nie, Y.; Budnick, J. I.; Wells, B. O.; Sinkovic, B. Impact of valence states on the superconductivity of iron telluride and iron selenide films with incorporated oxygen. *Phys. Rev. B* **2012**, *85*, No. 214517.
(68) Wagner, C. D.; Riggs, W. M.; Davis, L. E.; Moulder, J. F.; Muilenberg, G. E., Eds.; *Handbook of X-Ray Photoelectron Spectroscopy: A Reference Book of Standard Spectra for Identification and Interpretation of XPS Data*; Perkin-Elmer Corp., Physical Electronics Division: Minnessota, USA, 1979.
(69) Brun, M.; Berthet, A.; Bertolini, J. C. XPS, AES and Auger parameter of Pd and PdO. *J. Electron Spectrosc. Relat. Phenom.* **1999**, *104*, 55−60.
(70) Kim, K. S.; Gossmann, A. F.; Winograd, N. Application of ESCA to the Study of Heterogeneous Catalysis: The Adsorption of O_2 and. *CO on a Silver Surface* **1974**, *46*, 197−200.
(71) Briggs, D.; Seah, M. P. In *Practical Surface Analysis*, 2nd ed.; Vol. 1: Auger and X-ray photoelectron spectroscopy; John Wiley and Sons: 1988.
(72) Bafekry, A.; Faraji, M.; Karbasizadeh, S.; Abdolhosseini, S. I.; Jappor, H. R.; Ghergherehchi, M.; Gogova, D. Two-dimensional FeTe2 and predicted Janus FeXS (X: Te and Se) monolayers with intrinsic half-metallic character: tunable electronic and magnetic properties via strain and electric field. *Phys. Chem. Chem. Phys.* **2021**, *23*, 24336−24343.
(73) Jobic, S.; Brec, R.; Rouxel, J. Anionic Polymeric Bonds in Transition Metal Ditellurides. *J. Solid State Chem.* **1992**, *96*, 169−180.
(74) Zhang, Y.; Liu, X.; Li, H.; Wang, C.; Zhao, J.; Zhang, W.; Chen, L. Steric Effect Induced Structural Phase Transition from Low-Symmetry Layered to High-Symmetry Cubic in Alloyed Tellurides. *Adv. Mater.* **2020**, *32* (15), 2001234.
(75) Liu, Y.; Yang, Z.; Zhang, X.; Li, J.; Wang, C.; Chen, L.; Zhang, W. Suppression of Peierls Distortion and the Emergence of a Rocksalt Phase in GeTe via Sn Alloying. *Nat. Commun.* **2022**, *13*, 2053.
(76) Sanna, S.; Neubauer, D.; Geisler, B.; Kliemt, K.; Krellner, C.; Wirth, S.; Steglich, F.; Nicklas, M. ∗f∗-Electron-Induced Symmetry Breaking in $CeAuBi_2$: A Route to High-Symmetry Quantum Materials. *Nat. Mater.* **2019**, *18*, 1196−1201.
(77) Posysaev, S.; Miroshnichenko, O.; Alatalo, M.; Le, D.; Rahman, T. S. Oxidation states of binary oxides from data anlytics of the electronic structure. *Comput. Mater. Sci.* **2019**, *161*, 403−414.
(78) Loi, F.; Pozzo, M.; Sbuelz, L.; Bignardi, L.; Lacovig, P.; Tosi, E.; Lizzit, S.; Kartouzian, A.; Heiz, U.; Larciprete, R.; Alfè, D.; Baraldi, A. Breakdown of the correlation between oxidation states and core electron binding energies at the sub-nanoscale. *Appl. Surf. Sci.* **2023**, *619*, No. 156755.
(79) García-Romeral, N.; Keyhanian, M.; Morales-García, Á.; Illas, F. Relating X-ray photoelectron spectroscopy data to chemical bonding in MXenes. *Nanoscale Adv.* **2021**, *3*, 2793−2801.

https://doi.org/10.1021/acs.inorgchem.5c02764
Inorg. Chem. 2025, 64, 23825−23833